

# **An integrated method for assessing vulnerability of buildings caused by debris flows in mountainous areas**

Chenchen Qiu<sup>1</sup>, Xueyu Geng<sup>1\*</sup>

<sup>1</sup>School of Engineering, University of Warwick, Coventry, CV4 7AL, UK

Xueyu Geng (**Corresponding Author**):

E-mail: [xueyu.geng@warwick.ac.uk](mailto:xueyu.geng@warwick.ac.uk)

School of Engineering, University of Warwick, Coventry, CV4 7AL, UK

**Abstract:** The vulnerability assessment of buildings in future scenarios is critical to decrease potential losses caused by debris flows in mountainous areas due to the complex topographical condition that could increase the environmental vulnerability to climate change. However, the lack of reliable methods limits the accurate estimation of physical damage and the associated economic loss. Therefore, an integrated method of physical vulnerability matrix and machine learning model was developed to benefit the estimation of damage degree of buildings caused by a future debris-flow event. By considering the building structures (reinforced-concrete (RC) frame and non-RC frame), spatial positions between buildings and the debris-flow channels (horizontal distance (*HD*) and vertical distance (*VD*)), and impact pressure ( $P_t$ ) to buildings, a physical vulnerability matrix was proposed to link physical damage with the four factors. In order to overcome the difficulty in estimating the possible impact pressure to buildings, an ensemble machine learning (ML) model (XGBoost) was developed with the involvement of geological factors. Additionally, the *HD* and *VD* were decided based on the satellite images. The Longxihe Basin, Sichuan, China was selected as a case study. The results show that the ML model can achieve a reliable impact pressure prediction because the mean absolute percentage error (MAPE), root mean squared error (RMSE) and mean absolute error (MAE) values are 9.53%, 3.78 kPa, and 2.47 kPa. Furthermore, 13.9% of buildings in the Longxihe Basin may suffer severe damage caused by a future

24 debris-flow event, and the highest economic loss is found in a residential building, reaching  $5.1 \times 10^5$  €.

25 Overall, our work can provide scientific support for the site selection of future constructions.

26 **Keywords:** Debris flow, geological factors, building, machine learning, vulnerability assessment

## 27 **1. Introduction**

28 Debris flows are among the most frequent and costly natural hazards due to climate change and  
29 difficulty in timely warning (Santi et al., 2011). These events can devastate entire settlements in their  
30 path and pose significant threat to natural environment (Immerzeel et al., 2020), causing destruction of  
31 aquatic biodiversity, along with damage to properties and finally leading to considerable economic  
32 losses worldwide each year (Qiu et al., 2022; Alene et al., 2024; Sridharan et al., 2024). In European  
33 Alps, this disaster claimed an economic loss of at least 5 € billion from 1988 to 2012 (Fuchs, 2009;  
34 Guzzetti et al., 2005). Moreover, a similar average annual loss is also found in China, approximately  
35 0.17 € billion of annual loss was recorded during the time period of 2005 and 2015 (Miao and Liu, 2020).  
36 In this case, a reliable estimation of the potential economic loss caused by debris flows is essential since  
37 it can provide guidance for decision-makers about where to place the infrastructures and buildings. The  
38 buildings are the most susceptible element to debris flows, and they are responsible for most of the  
39 economic loss (Fuchs, 2009; Wei et al., 2018). Therefore, in order to calculate the potential economic  
40 loss, it is critical to estimate the damage degree of the buildings since economic loss is linked to the  
41 physical vulnerability of a property and its economic value.

42 The physical vulnerability quantifies the damage degree of a property, and the methods that are used  
43 to decide the physical vulnerability include mechanical method (Ruggieri et al., 2023, 2022),  
44 vulnerability matrices, vulnerability curves, vulnerability indicators (Papathoma-Köhle et al., 2017). The  
45 mechanical methods derive the vulnerability functions of buildings based on numerical models, which  
46 may achieve relatively high evaluation accuracy but highly rely on controlled laboratory experiments to  
47 obtain input data. As a result, this method itself is time-consuming and costly for regional application  
48 (Paudel et al., 2021; Qiu et al., 2022). Three vulnerability curves were derived using numerical  
49 modelling to relate the vulnerability to debris-flow intensity, including flow height, flow velocity, and

50 kinematic viscosity (Quan Luna et al., 2011). Although these three curves can suggest the physical  
51 vulnerability of a building at risk but fail to consider the impacts of building structures on damage  
52 degree. Therefore, a brick structure and a reinforced-concrete frame were included in the development of  
53 vulnerability curves by Zhang et al. (2018). However, the involvement of limited building types restricts  
54 the application of the curves when the determination of physical vulnerabilities for different building  
55 types is required. Therefore, considering the limitations of vulnerability curves, different vulnerability  
56 matrixes of buildings have also been developed by many studies due its advantages in interaction  
57 understanding between the debris-flow process and elements at risk and easily readable by non-experts  
58 (Bründl et al., 2009; Kang and Kim, 2016; Zanchetta et al., 2004). In contrast, these developed matrixes  
59 ignored the spatial position (horizontal distance and vertical distance) between the buildings and the  
60 debris-flow channels, which would misestimate the damage degree of a building caused by a debris-flow  
61 event. As for the vulnerability indicators, this method considers the characteristics of buildings without  
62 relating the debris-flow process when evaluating the damage degrees (Fuchs et al., 2019). Therefore, it is  
63 crucial to establish a comprehensive assessment matrix that takes into account the structural types,  
64 spatial positions between buildings and the debris-flow channels, and debris-flow intensities to estimate  
65 the potential damages of the buildings. Additionally, the possible damage degree of the buildings in  
66 future scenarios was not considered by the past studies (Papathoma-Köhle et al., 2017). Therefore, this  
67 study focuses on conducting an assessment of the potential physical damage of a building due to a future  
68 debris-flow event.

69       Among the four factors in deciding the physical damage of buildings (building structure, spatial  
70 locations ( $HD$  and  $VD$ ), and impact pressure ( $P_i$ )), impact pressure remains an unsolved problem since  
71  $HD$  and  $VD$  can be determined based on the satellite images. In this case, a machine learning model was  
72 developed to predict the impact pressure to a building because this method can uncover intricate and

73 concealed relationships between various input variables and an output result (Khosravi et al., 2021; Jiang  
74 et al., 2023). To leverage the benefits of rapid processing and handling large-scale data, we employ an  
75 ensemble model, specifically extreme gradient boosting (XGBoost). This choice is made due to  
76 XGBoost's ability to partition data into smaller components, facilitating parallel computation and  
77 multithreading to enhance processing speed (Chen and Guestrin, 2016).

78 In this paper, we proposed an integrated method of physical vulnerability matrix and machine  
79 learning model to estimate the physical damage of a building caused by a future debris-flow event,  
80 finally estimating the economic loss of this property. The buildings in the Longxihe Basin, Sichuan,  
81 Chian, were extracted to conduct a case study to test the efficiency and reliability of this method in  
82 physical damage estimation and corresponding economic loss. The formation of terrain in this area is  
83 affected by severe tectonic activities, such as earthquakes (Chang et al., 2014; Chang et al., 2015), which  
84 can produce abundant loose materials for potential debris flows.

## 85 **2. Methodology**

86 To estimate the economic loss of buildings caused by a future debris-flow event, several steps are  
87 comprised in this study (see Fig. 1):

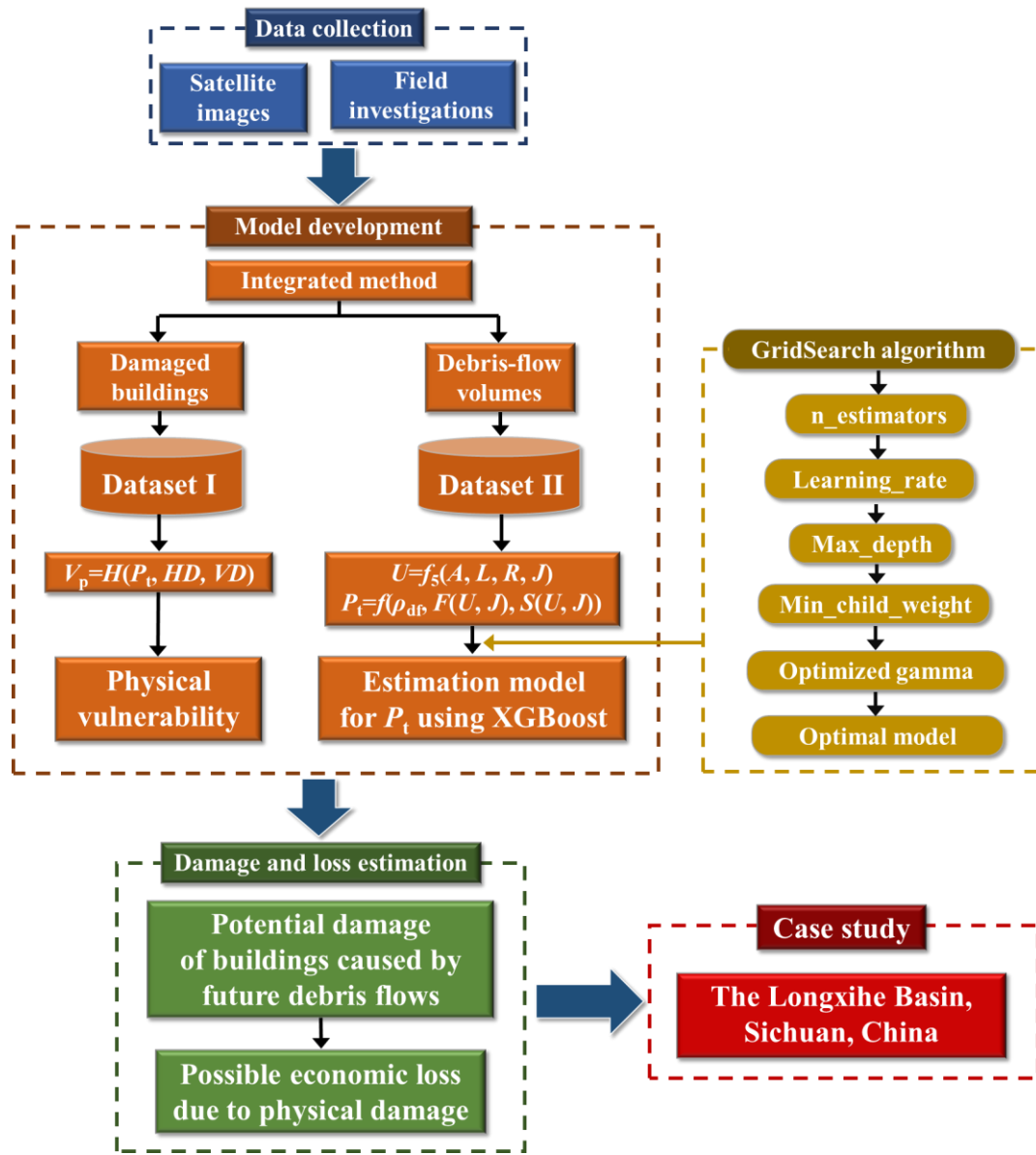


Figure 1. Flow chart of this study

88

89

90

91

92

93

94

95

96

97

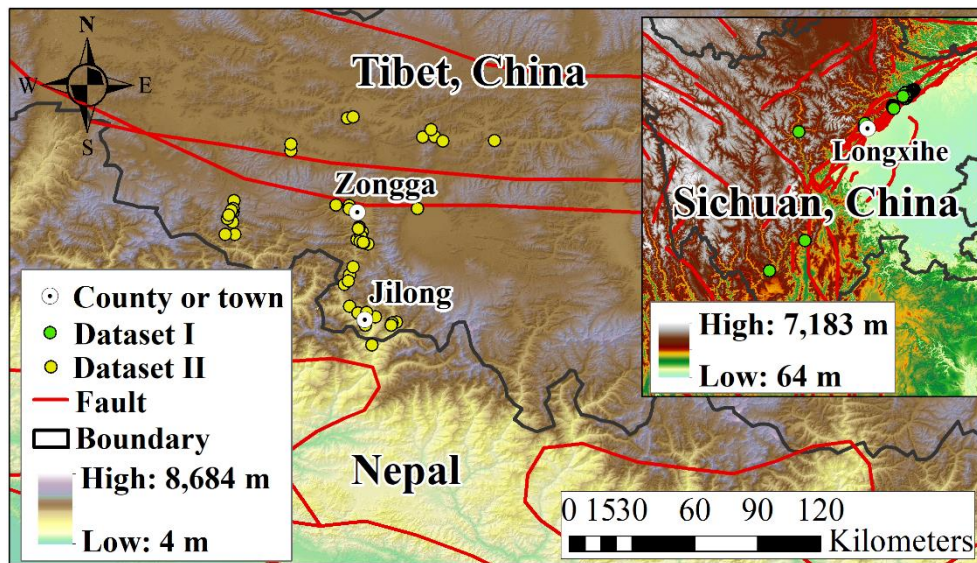
(1) The historical debris-flow events in Gyirong, Tibet Tibetan Autonomous Region, and the Sichuan Basin (Fig. 2) from the past ten years were investigated based on satellite images and field investigations to collect information regarding the debris-flow volumes and damaged buildings.

(2) We categorized the collected historical debris flows into two datasets (dataset I and dataset II) for the development of a physical vulnerability matrix and a prediction model, respectively.

(3) The dataset I includes the debris-flow events that caused damages to the buildings. In detail,  $V_p$  is the physical vulnerability of buildings, and  $P_t$  represents the impact pressure of a debris-flow event to buildings.  $HD$  and  $VD$  are horizontal and vertical distance of buildings to their nearest debris-flow

98 channel. Therefore, this dataset is employed for the development of a physical vulnerability matrix. This  
99 dataset mainly includes the debris-flow events occurred in the Sichuan Basin, China and also several  
100 events in the Gyirong areas.

101 (4) The dataset II is composed of the debris-flow events that occurred in areas without the  
102 distribution of buildings, and, therefore, no property loss is caused by these events. For the purpose of  
103 establishing an estimation model, a series of factors, such as the depositional volume of a debris-flow  
104 event ( $U$ ), area of a debris-flow catchment ( $A$ ), length of the main channel for a catchment ( $L$ ), the  
105 average topographic relief ( $R$ ), and the average gradient of main channel ( $J$ ).  $\rho_{df}$  is the mean density of  
106 the material. Therefore, this dataset was used for model training and utilize this model to estimate the  
107 debris-flow intensity in future scenarios, such as debris-flow impact pressure to buildings. This dataset is  
108 shown in Table A1 of Appendix. A.



109  
110 Figure 2. The collected historical debris flows in the Tibet Plateau and the Sichuan Basin

## 111 2.1 Physical vulnerability matrix

112 Vulnerability, usually referring to physical vulnerability, denotes the extent of damage a property  
113 may suffer when subjected to a hazard event, such as a landside and a debris-flow event (Fell, 1994),  
114 ranging from no damage (vulnerability is assigned as 0) to completely destroyed (vulnerability is

115 assigned as 1). To obtain the future economic loss of a building at risk, a physical vulnerability matrix of  
 116 the buildings was proposed. The determination of physical vulnerability ( $V_p$ ) relied on the impact  
 117 pressure ( $P_t$ ) to buildings, the horizontal distance ( $HD$ ), and the vertical distance ( $VD$ ) between the  
 118 building and the nearest debris-flow channel, as indicated by Eq. (1). The determination details of the  
 119 three parameters in Eq. (1) are demonstrated in the following sections.

$$120 \quad V_p = H(P_t, HD, VD) \quad (1)$$

### 121 **2.1.1 Calculation of impact pressure**

122 In order to propose a physical vulnerability matrix, the first step is to link the impact pressure to  
 123 damage degree. As suggested by Jakob et al. (2012) and Kang and Kim (2016),  $P_t$  can effectively reflect  
 124 the energy of debris flows and possible damage degree of buildings. However, past studies usually  
 125 utilized debris-flow magnitude to decide the physical vulnerability since a greater magnitude may  
 126 indicate a more significant impact force (Dai et al., 2002). This impact force cannot represent the actual  
 127 damage of a building during a debris-flow event because the catchment with a potential large-scale  
 128 debris-flow event may not cause severe damage to the buildings. The reason behind this uncertainty  
 129 could be due to the moderate gradient of debris-flow channel and its frictional resistance, which could  
 130 decrease the kinetic energy of the travelling mass (Qiu et al., 2024). Consequently, only a slight or  
 131 moderate damage to buildings could be caused. Therefore, impact pressure can better reflect the damage  
 132 degree of buildings when subjected to different debris-flow magnitudes, which can be calculated through  
 133 considering the dynamic overpressure and hydrostatic pressure (Eq. (2)) (Zanchetta et al., 2004):

$$134 \quad P_t = \frac{1}{2} \rho_{df} gh + \rho_{df} v^2 = f(\rho_{df}, h, v) \quad (2)$$

135 where  $P_t$  (kPa) represents the impact pressure to buildings, and  $g$  is the gravitational acceleration.  $v$  (m/s)  
 136 represents the flow velocity at the maximum discharge, and  $\rho_{df}$  is the mean density of materials for a  
 137 debris-flow event.  $h$  (m) is the flow depth that describes the deposit depth on buildings. As for the



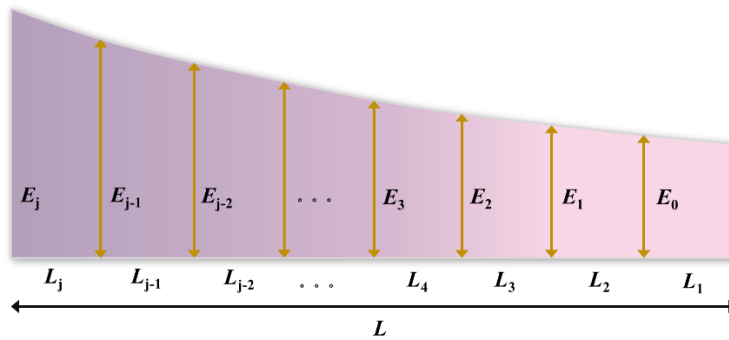
138 debris-flow velocity ( $v$ ) at peak discharge ( $Q_p$ ), it can be calculated using the equation proposed by  
 139 Rickenmann (1999). This equation considers the debris-flow datasets in different regions, such as Italy,  
 140 China, Japan, U.S.A, and Columbia, which enables its feasibility to be used in wider and different areas.

$$141 \quad v = 2.1Q_p^{0.33} J^{0.33} = f_1(Q_p, J) \quad (3)$$

142 This equation illustrates that the velocity can be decided by  $Q_p$  ( $m^3/s$ ) and channel gradient ( $J$ ) (Cui  
 143 et al., 2013). It's worth noting that  $J$  changes along the channel. In our study, we focused on the mean  
 144 gradient of the main channel within a debris-flow catchment, and it is calculated using the equation  
 145 proposed by IMHE (1994):

$$146 \quad J = \frac{\left( \sum_{j=1}^m (E_{j-1} + E_j) L_j - 2E_0 L \right)}{L^2} \quad (4)$$

147 where  $J$  is the mean path gradient (‰).  $E_j$  ( $j=1, 2, \dots, j-1$ ) represents the elevation of each break point in  
 148 the movement path (m). Elevation was downloaded from the ASF website  
 149 (<https://search.asf.alaska.edu/#/>) that can provide DEM with a spatial resolution of 12.5 m.  $L_j$  is length  
 150 of each section within the movement path (m).  $m$  is the number of sections.  $E_0$  represents the elevation  
 151 at the endpoint of the mass movement (m), while  $L$  denotes the length of the travel path (m). The divided  
 152 sections are presented in Fig. 3.



153  
 154 Figure 3. The segments of main channel within a catchment

155 The calculation of  $Q_p$  can be determined based on the equation (Eq. (5)):

$$156 \quad Q_p = (U / 152.97)^{1/1.266} = f_2(U) \quad (5)$$

157 Therefore, the  $Q_p$  can be calculated based on the estimated volume ( $U$  ( $m^3$ )) of historical debris

158 flows. However, the absence of flow depth ( $h$ ) also hampers the calculation of impact pressure.  
 159 Therefore, an equation is used to calculate the flow depth (Koch, 1998). This formula has been proven to  
 160 perform well in the numerical simulation of viscous debris flows (Eq. (6)):

$$161 \quad h = \left( v / C_1 J^{0.5} \right)^{10/3} = f_3(v, C_1, J) = f_3\left(f_1(Q_p, J), C_1, J\right) \quad (6)$$

162 where  $C_1$  represents the dimensional empirical coefficient. This value of parameter is indicated by a  
 163 semi-theoretical relationship (Eq. (7)) (Rickenmann, 1999):

$$164 \quad C_1 = 10Q_p^{2/25} = f_4(Q_p) = f_4(f_2(U)) \quad (7)$$

165 Therefore, the impact pressure can be described as a function of debris-flow volume and channel  
 166 gradient, and the impact pressures of dataset I are calculated based on Eqs. (2)-(7) (see Table 1).**2.1.2**

### 167 **Determination of $HD$ and $VD$ values**

168  $HD$  and  $VD$  values were also introduced here since the actual damage will be significant if a  
 169 building stands close to the debris-flow channel (Sturm et al., 2018). They can be estimated through  
 170 high-resolution satellite images, such as Gaofen, Ziyuan, WorldView, and GeoEye. In this study,  
 171 Gaofen-2 satellite images are employed for determining the  $HD$  and  $VD$  values. This satellite can  
 172 capture panchromatic (black and white) images with a spatial resolution reaching 0.8 m and  
 173 multispectral (color) images with a spatial resolution up to 3.2 m. Therefore, the resolution of satellite  
 174 images used for determination of  $HD$  values is 0.8 m. However, there is no elevation information  
 175 provided by satellite images. Therefore, DEM was used to extract the  $VD$  information between building  
 176 and its nearest debris-flow channel. As for the building clusters that are hard to be separated into  
 177 individual buildings manually, a ‘fishnet’ tool in GIS was used to automatically divide these clusters into  
 178 building segments. Furthermore, the rectangle segments were converted into points so that each point  
 179 represents a building. As a result, the  $HD$  and  $VD$  values of a building can be decided. The damaged  
 180 buildings are mainly distributed on the accumulation fans. Therefore, even though a large  $HD$  is

181 observed, the  $VD$  is small due to the mild slope and smooth topography of the alluvial fans (Marcato et  
 182 al., 2012). By considering the impact pressure,  $HD$ , and  $VD$  values, a physical vulnerability matrix can  
 183 be established to evaluate the physical damage of a building caused by a debris-flow event.

## 184 2.2 Economic loss of a building at risk

185 The economic loss of a building caused by a debris-flow event can be estimated based on  
 186 multiplication of its physical vulnerability and economic value.

$$187 \quad V_e = V_p \times M = H(P_t, HD, VD) \times M; M = P \times A \quad (8)$$

188 where  $V_e$  and  $M$  represent the economic loss and the economic value of a building, respectively.  $P$  is the  
 189 unit price of a building, and  $A$  represents the area of a building. Therefore, estimating  $V_p$  holds  
 190 paramount importance in estimating economic loss. However,  $V_p(H(P_t, HD, VD))$  is represented by the  
 191 proposed physical vulnerability matrix. In this context, determining  $P_t$  plays a critical role in economic  
 192 loss estimation. Therefore, to forecast the possible economic loss caused by a future debris-flow event,  
 193 we need to estimate the impact pressure to buildings caused by a future debris-flow event.

## 194 2.3 Prediction model development

195 To predict the future impact pressure to buildings when a debris-flow event occurs, determining  
 196 factors is essential. Therefore, we further developed Eq. (6) by integrating Eq. (5) and Eq. (7) to this  
 197 equation:

$$198 \quad h = f_3(f_1(f_2(U), J), f_4(f_2(U)), J) = F(U, J) \quad (9)$$

199 Additionally, Eq. (3) can be rewritten as:

$$200 \quad v = f_1(Q_p, J) = f_1(f_2(U), J) = S(U, J) \quad (10)$$

201 Therefore, the determination of impact pressure relies on  $U$  and  $J$ :

$$202 \quad P_t = f(\rho_{df}, F(U, J), S(U, J)) \quad (11)$$

203 However, the debris-flow volume is closely related to a set of geomorphic factors, as suggested by

204 Huang et al. (2020). They are catchment area ( $A$ ), channel length ( $L$ ), topographic relief ( $R$ ), and mean  
 205 slope of the main channel ( $J$ ). The catchment area can reflect the debris availability and capacity of  
 206 generating and containing the volume of loose materials for a debris-flow catchment. As for the channel  
 207 length, it is related to the entrained and transported sediment volume (Marchi et al., 2019). Therefore,  
 208 this parameter can also impact the final volume of a debris-flow event.  $R$  is defined as the terrain  
 209 fluctuation and roughness of a catchment. To calculate this value, we need to first decide the optimal  
 210 statistical unit in this area using the change-point model. Then, the subtraction value between the  
 211 maximum value and minimum values of an optimal statistical unit is calculated. Finally, we utilized the  
 212 maximum subtraction value to represent the  $R$  value of a catchment.  $J$  is defined as the ratio of the  
 213 elevation difference of the main channel and channel length. A longer distance could be achieved for a  
 214 debris-flow event if a steep channel exists in a catchment (de Haas and Densmore, 2019). In this case,  $U$   
 215 can be described as a function of  $A$ ,  $L$ ,  $R$ , and  $J$ :

$$216 \quad U = f_5(A, L, R, J) \quad (12)$$

217 Furthermore, substituting Eq. (12) to Eq. (11):

$$218 \quad P_t = f(\rho_{df}, F(f_5(A, L, R, J), J), S(f_5(A, L, R, J), J)) \quad (13)$$

219 Therefore,  $P_t$  can be described as a complex function of geomorphology-related factors, including  $A$ ,  
 220  $L$ ,  $R$ , and  $J$ . To find the complicated correlations among them, an ensemble machine learning model  
 221 (extreme gradient boosting (XGBoost)) was employed here to establish the relationship and then utilize  
 222 this relationship to estimate the potential impact pressure to buildings when a future debris-flow event  
 223 occurs. The basic mechanism of XGBoost is to constantly develop a new decision tree which acts as a  
 224 weak learner and fits the residual error of the last prediction. After the training of a total of  $k$  trees, the  
 225 final prediction result is the sum of the score of each leaf node in each developed tree. In this study,  
 226 GridSearch algorithm was employed to decide the optimal hyper-parameters of XGBoost. As a result,

227 the hyper-parameters, such as  $n\_estimators$ ,  $learning\_rate$ ,  $max\_depth$ ,  $min\_child\_weight$ , and  $gamma$ ,  
 228 were decided as 500, 0.1, 5, 1, and 0.01, respectively. Overall, the target function of regression is placed  
 229 in Appendix. A. Additionally, the database II that is used for impact pressure prediction is presented in  
 230 Table A1 of Appendix. A.

## 231 2.4 Model assessment

232 After the impact pressure prediction, three assessment indexes were used to evaluate the prediction  
 233 performance, including MAPE (Mean Absolute Percentage Error), RMSE (Root Mean Square Error),  
 234 and MAE (Mean Absolute Error):

$$235 \quad MAPE = \frac{1}{m} \sum_{i=1}^m \frac{|y_i - y_{ipre}|}{y_i} \quad (14)$$

$$236 \quad RMSE = \sqrt{\frac{1}{m} \sum_{i=1}^m (y_i - y_{ipre})^2} \quad (15)$$

$$237 \quad MAE = \frac{1}{m} \sum_{i=1}^m |y_i - y_{ipre}| \quad (16)$$

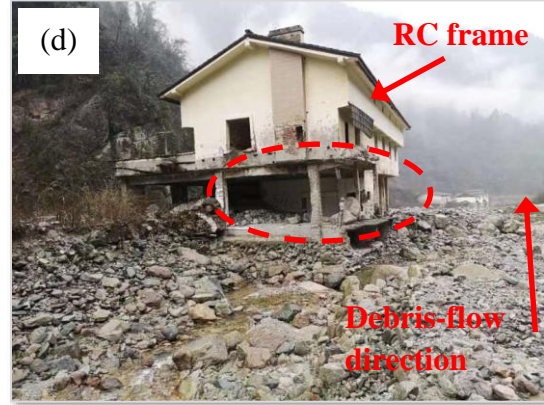
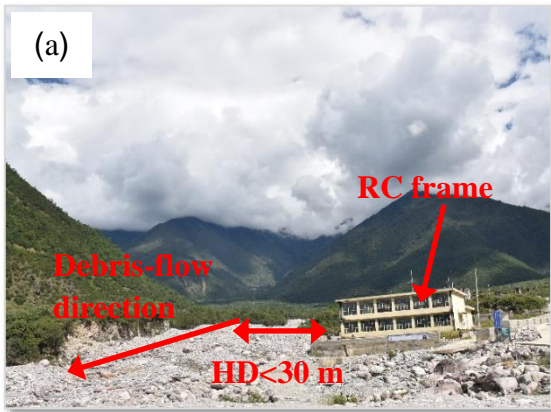
238 where  $y_i$  is the actual value, and  $y_{ipre}$  represents the prediction value.  $m$  is the number of prediction  
 239 values.

## 240 3. Result analysis

### 241 3.1 The relationship between the damage degree and $P_t$

242 Fig. 3 shows the different damage degrees of buildings in dataset I. The buildings were classified  
 243 into two types, including RC-frame (reinforced concrete) and non-RC frame (masonry, wooden structure,  
 244 and light steel frame). As indicated in Figs. 4(e)-(f), The masonry buildings suffer severe damage, and  
 245 the light steel frame buildings and wooden structure buildings are destroyed (Figs. 4(g)-(h)) even though  
 246 the impact pressure to buildings was estimated to be less than 30 kPa. However, the main structure of  
 247 the reinforced concrete building can stay undamaged (Fig. 4(b)) when severe damage is found on the  
 248 masonry structure (see a dashed circle in Fig. 4(b)) during the same debris-flow event. This resistance

249 ability difference indicates the difference in physical vulnerabilities between the RC and the non-RC  
250 frames, which can also be seen in Fig. 4(a). Moreover, moderate damage to the RC frame with  
251 unreinforced masonry infill walls is found in Fig. 4(c) when a small-scale debris-flow event occurs.  
252 Additionally, the RC frame suffers extensive damage when the impact pressure exceeds 100 kPa based  
253 on the estimated debris-flow volume. Therefore, the identifications of different damage degrees for  
254 buildings provide us with access to proposing a classification standard for the physical vulnerability of  
255 buildings.



256

257

258





259

260 Figure 4. Photographs of the damaged residential buildings caused by debris flows during the field  
261 investigations on the Qinghai-Tibetan Plateau

### 262 3.2 Determination of *HD* and *VD* thresholds

263 The field investigations and statistical results show that the non-RC frame buildings are destroyed or  
264 suffer structural damage when the *HD* is less than 30 m (Fig. 5(a)). The damaged buildings cannot be  
265 repaired, and reconstruction is required. In consistent with the conclusion of past study (Wei et al., 2022),  
266 the residential buildings, such as brick structures (Fig. 5(b)) and the RC frame buildings (Fig. 5(c)), are  
267 partially buried by the debris-flow sediments without structural damage when the *HD* is greater than 100  
268 m but less than 160 m. Therefore, 160 m is another *HD* threshold to classify the inundated and slightly  
269 affected areas. The upper limit of *HD* value for the historical debris flows during the field investigations  
270 is 230 m because almost 94% of *HD* values are less than 230 m (see Table 1).

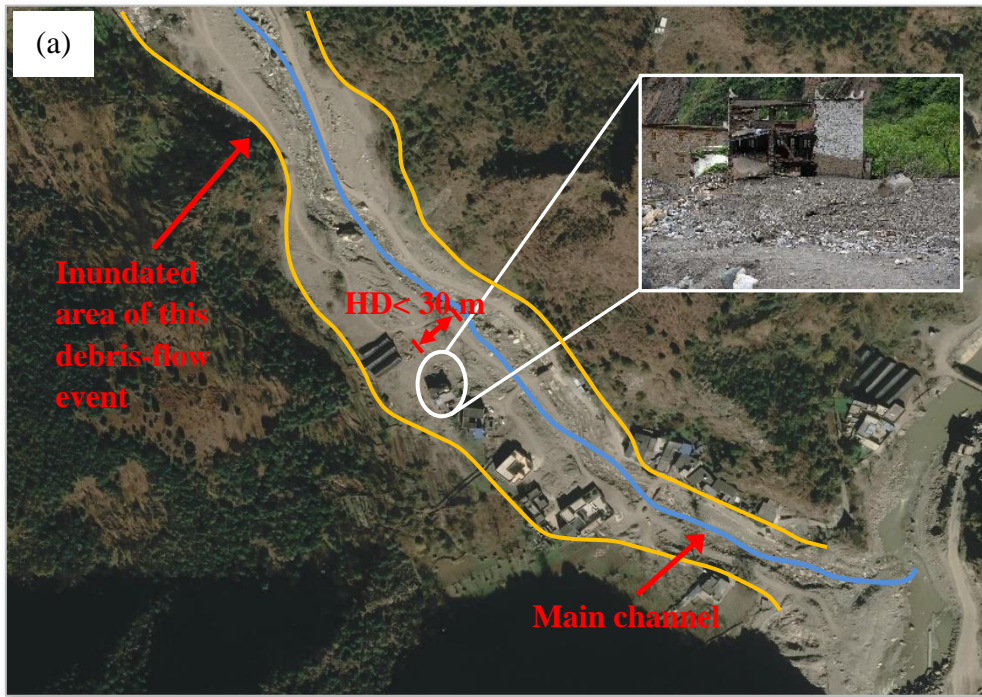


Figure 5. Examples of the determination of the  $HD$  thresholds

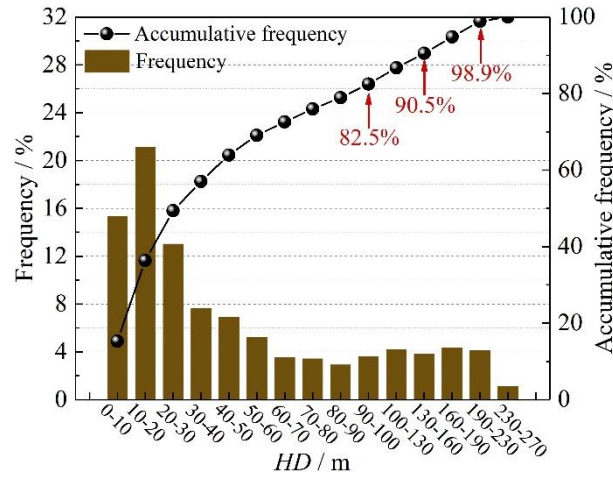
**Table 1.** Dataset I for physical vulnerability matrix.

No.	Year	Lon (°)	Lat (°)	Number of damaged buildings	Impact pressure $P_t$ (kPa)	Maximum $HD$ (m)	Maximum $VD$ (m)
1	2006	85.3278	28.3735	21	16.1	162	12
2	2007	85.5683	29.1875	13	40.6	141	12
3	2007	85.5528	28.8717	7	37.5	13	7
4	2008	85.6241	29.1869	21	41.0	119	3
5	2010	86.0872	29.1625	11	35.5	54	2
6	2013	85.3112	28.7649	53	24.1	284	29
7	2015	85.2928	28.4174	9	117.4	160	2
8	2015	85.3608	28.4074	22	31.1	131	107
9	2015	85.3542	28.7159	7	17.5	82	13
10	2015	84.7653	28.7559	38	132	74	15



11	2015	85.4566	28.3868	3	5.1	32	10
12	2015	85.4413	28.3827	1	32.7	17	6
13	2015	85.0105	29.1208	3	5.2	133	2
14	2015	85.2579	29.2603	9	9.8	146	2
15	2015	85.2759	29.2652	6	14.8	228	10
16	2015	85.0083	29.1493	4	14.6	171	3

275 In order to support the thresholds determination of  $HD$ , we further analyzed the frequencies of  $HD$   
276 values for the damaged buildings, as depicted in Table 1, through dividing the  $HD$  values into several  
277 intervals. The frequency and accumulative frequency results are shown in Fig. 6.



278  
279 Figure 6. The frequency and accumulative frequency distributions of the 228 damaged buildings.

280 As depicted in Fig. 6, the highest proportion occurs in the range of 10 to 20 m, accounting for 20.1%,  
281 followed by a 15% percentage of  $HD$  values falling between 20 to 30 m. Therefore, the proportion  
282 falling within the range of 0 to 30 m is 49.4%, and approximately 82.5% of the  $HD$  values is measured  
283 under 100 m. Following the suggestion of Liu et al. (2020), a probability of 50% is considered a  
284 threshold for debris-flow warning, which implies that 30 m in this study can serve as a threshold.  
285 Moreover, the accumulative frequency of 80% is selected as another threshold based on Wei et al. (2018),  
286 corresponding to the  $HD$  value of 100 m. Furthermore, 90.5% of the damaged buildings have  $HD$  value  
287 less than 160 m, and nearly 98.9% of the damaged buildings fall within the  $HD$  range of 0 to 230 m. As  
288 a result, 160 m and 230 m are selected as additional two thresholds. In addition to the determination of  
289  $HD$  threshold values, the maximum flow depth ( $h_{max}$ ) in the debris-flow channel is used as a reference to  
290 decide the  $VD$  thresholds since the buildings are mostly situated along the channels (Fig. 5(a) and Fig. 7).

291 Therefore, calculating the elevation difference between the buildings and the nearest debris-flow  
292 channel is critical to evaluate the safety of the buildings. It's worth noting that the height of a building  
293 was not considered when estimating the  $VD$  values. For example, both the masonry buildings in Fig. 5(a)  
294 and Fig. 7 are close to the debris-flow channel. However, no severe damage is observed for the building  
295 in Fig. 7 because it has a considerable vertical distance from the main channel. To decide the  $VD$   
296 thresholds, the  $h$  values of the historical debris flows are presented in Table A1 of Appendix. A. The  
297 average depth of the debris flows is 2.6 m, and nearly all the  $VD$  values are less than 4 m. Therefore, 4 m  
298 serves as the first threshold, suggesting that the most severe damage to the buildings may be caused  
299 when the  $VD$  is less than 4 m. Whilst a debris-flow depth value of as high as 10 m is suggested (Xie et  
300 al., 2013), which can be found in curved channels. Consequently, we utilize 10 m to indicate the  
301 moderate damage of buildings when the  $VD$  is less than 10 m but greater than 4 m. Moreover, a vertical  
302 distance of 14 m above the river level is considered to record the river gauging on the Iowa River using a  
303 digital video camera (Creutin et al., 2003), which indicates a safe  $VD$  value to avoid damage caused by  
304 the river discharge. Therefore, 15 m is used as the upper limit of the  $VD$  values in this paper.



305  
306 Figure 7. Example of the determination of the  $VD$  threshold, and  $VD$  in this figure indicates the height

307 difference between the river table and the masonry structure without considering the height of this  
 308 building.

### 309 3.3 Physical vulnerability matrix ( $h(P_t, HD, VD)$ )

310 The proposed physical vulnerabilities of residential buildings are listed in Table 2. Extensive  
 311 damage or even complete damage may occur when a non-RC building is located near the debris-flow  
 312 channel with  $HD$  less than 30 m and  $VD$  less than 4 m. However, a significant improvement in resistance  
 313 ability can be observed when the non-RC frame is replaced by the RC frame considering the same  
 314 impact pressure,  $HD$  and  $VD$  values. In general, the buildings hardly suffer damage when the  $VD$  is  
 315 greater than 10 m. Therefore, the economic loss of a building can be calculated based on the proposed  
 316 physical vulnerabilities and economic values.

317

Table 2. Physical vulnerability matrix

$P_t$ (kPa)	Building structure	$HD < 30$ m			$30 < HD < 100$ m		
		$4 < VD < 10$	$10 < VD < 15$	$15 < VD < 20$	$4 < VD < 10$	$10 < VD < 15$	$15 < VD < 20$
<30	RC frame	0.3	0.2	0.1	0.2	0.1	/
	Non-RC frame	0.8	0.7	0.6	0.7	0.6	0.4
30-70	RC frame	0.6	0.5	0.4	0.5	0.4	0.2
	Non-RC frame	1	0.9	0.8	0.9	0.8	0.6
70-100	RC frame	0.7	0.6	0.5	0.6	0.5	0.3
	Non-RC frame	1	1	0.9	1	0.9	0.7
>100	RC frame	0.8	0.7	0.6	0.7	0.6	0.4
	Non-RC frame	1	1	0.9	1	1	0.8
$P_t$ (kPa)	Building structure	$100 < HD < 160$ m			$160 < HD < 230$ m		
		$4 < VD < 10$	$10 < VD < 15$	$15 < VD < 20$	$4 < VD < 10$	$10 < VD < 15$	$15 < VD < 20$
<30	RC frame	0.1	/	/	/	/	/
	Non-RC frame	0.6	0.4	0.1	0.4	0.1	/
30-70	RC frame	0.4	0.2	/	0.2	/	/
	Non-RC frame	0.8	0.6	0.3	0.6	0.3	/
70-100	RC frame	0.5	0.3	/	0.3	/	/
	Non-RC frame	0.9	0.7	0.4	0.7	0.4	/
>100	RC frame	0.6	0.4	0.1	0.4	0.1	/
	Non-RC	1	0.8	0.5	0.8	0.5	0.1

### 3.4 Prediction model development and assessment

The debris flows in Table A1 (see Appendix. A) were divided into a training set and a validation set with a ratio of 7:3, and the training set is used to train the prediction model. The validation results are plotted in Fig. 8. Additionally, the performance of the developed model is assessed using the three indexes (Eqs. (14)-(16)). As indicated in Fig. 8, the prediction results show minor errors to the actual values, and the MAPE, RMSE and MAE values are 9.70%, 3.98 kPa and 2.74 kPa, respectively. RMSE value can reflect the extreme errors, and the calculated RMSE value can indicate that there are no extreme values observed in the prediction results. Additionally, MAPE reflects the error percentage between the measured and predicted values, and the model is more reliable if the MAPE is closer to 0. Therefore, it can be concluded that this model performed well in predicting the volume of a future debris-flow event.

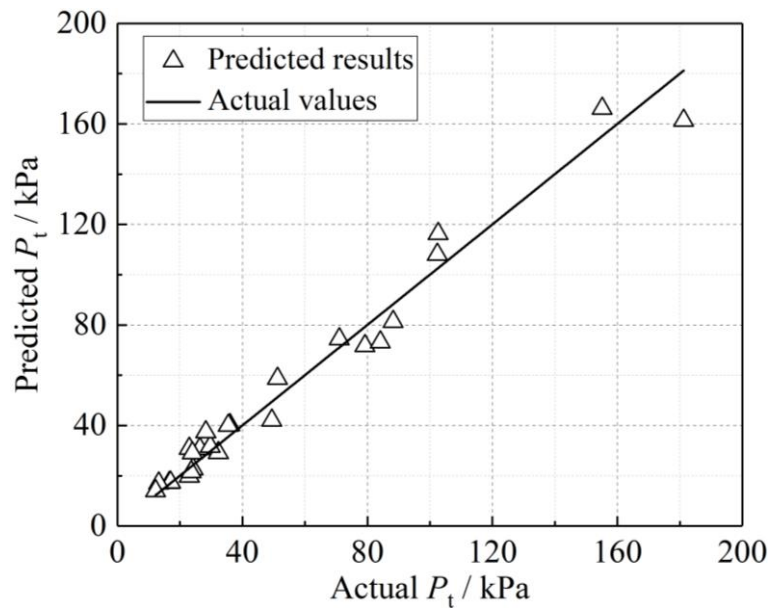


Figure 8. Plots of deviations between the prediction results in hollow triangle estimated by the machine learning model and actual values represented by a straight line

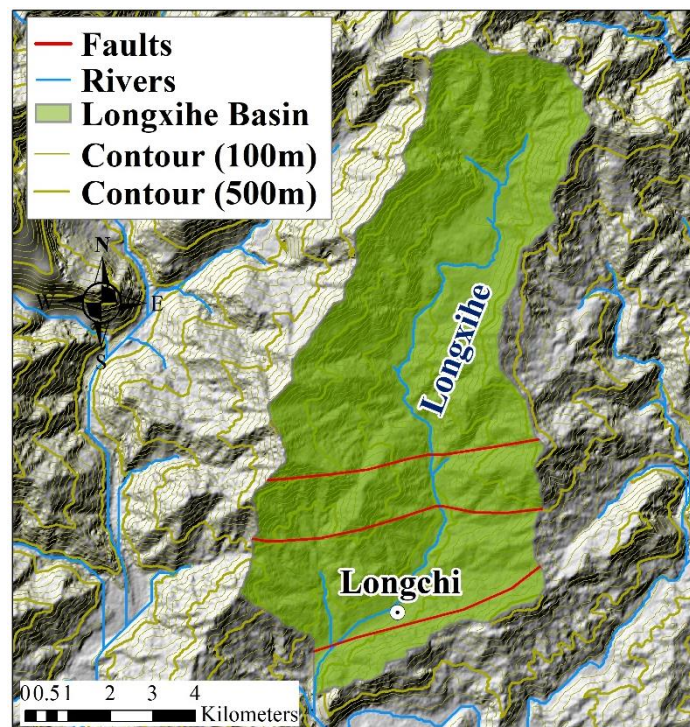
## 4 Case study

### 4.1 Geological setting

We selected the Longxihe Basin (Fig. 9) in Dujiangyan, Sichuan Province, to conduct a case study



335 (see Fig. 1 about the geographic location of this area), which is 15 km away from the epicenter of the  
336 2008 Wenchuan earthquake. There are three faults crossing this area, namely the Southern Branch of the  
337 Yingxiu-Beichuan Fault, the Northern Branch of the Yingxiu-Beichuan Fault, and the Feilaifeng  
338 Structure. These faults and structures cause the incised valleys and uplifting of the land surface, resulting  
339 in large areas of exposed rocks. Additionally, this study area belongs to the subtropical monsoon climate,  
340 with annual precipitation reaching 1,134.8 mm. Over 80 % of the annual rainfall occurs from May to  
341 September. Consequently, the abundant rainfall and complex geological structure give birth to frequent  
342 debris flows. It was reported that 13 debris-flow events occurred in this basin on 12<sup>th</sup> May, 24<sup>th</sup> June,  
343 25<sup>th</sup> September 2008, and 17<sup>th</sup> July 2009. In particular, 45 debris-flow events were recorded on 13<sup>th</sup>  
344 August 2010 due to a high-intense rainfall event, causing severe damage to 233 buildings and resulting  
345 in the entire economic loss of  $7.2 \times 10^7$  € (Yu et al., 2011). There are one town and two villages  
346 distributed in this basin. The impacts of the Wenchuan earthquake still pose threats to the local people  
347 since a time period of at least 20 years is required if the occurrence frequency of debris flows before the  
348 earthquake is expected (Yu et al., 2014).



349

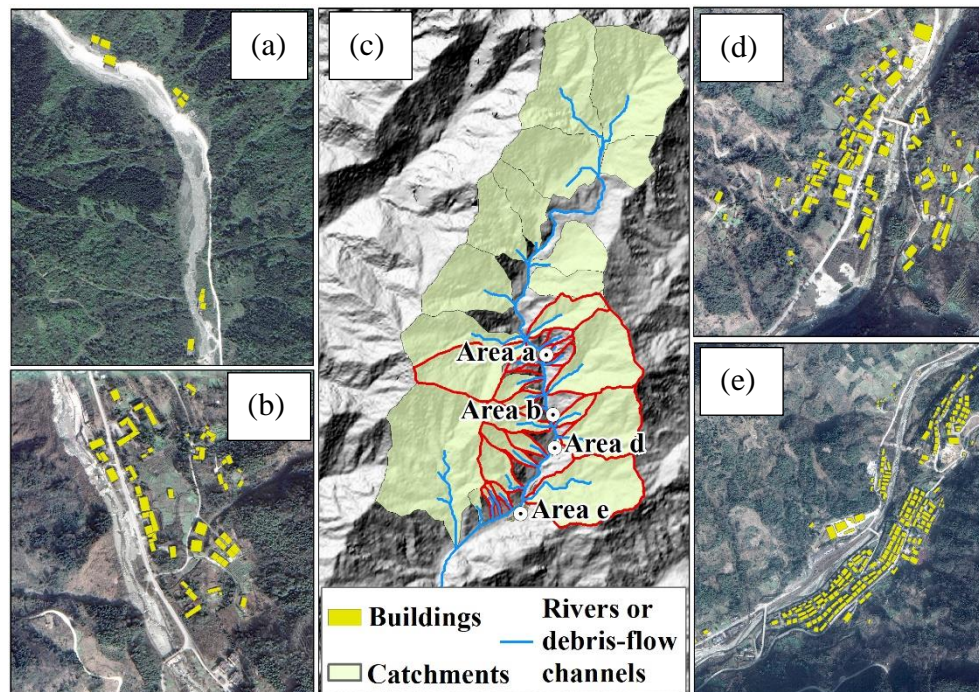
350 Figure 9. The Longxihe Basin located in north-western part of Dujiangyan, China with a total area of  
351 70.56 km<sup>2</sup> and elevation ranging from 794 m to 3,245 m.

## 352 4.2 Estimation of economic loss of buildings

### 353 4.2.1 Determination of physical vulnerability

354 To estimate the potential physical damage of the buildings in the Longxihe Basin, the developed  
355 prediction model was applied to predict the potential impact pressure to buildings. As illustrated in Fig.  
356 10(c), the debris-flow catchments within this basin were generated since we mainly focus on the regions  
357 with the distribution of buildings and estimate the possible economic loss of the buildings when debris  
358 flows occur. Therefore, we extracted a total of 386 buildings in three regions based on the Gaofen-2  
359 satellite images (Fig. 10(a), Fig. 10(b), Fig. 10(d), and Fig. 10(e)). After that, we selected the catchments  
360 that are the nearest to the buildings to conduct analysis (see highlighted catchments with red lines in Fig.  
361 10(c)). The input information of these catchments for impact pressure prediction and the predicted  
362 results are all listed in Table 3.

363



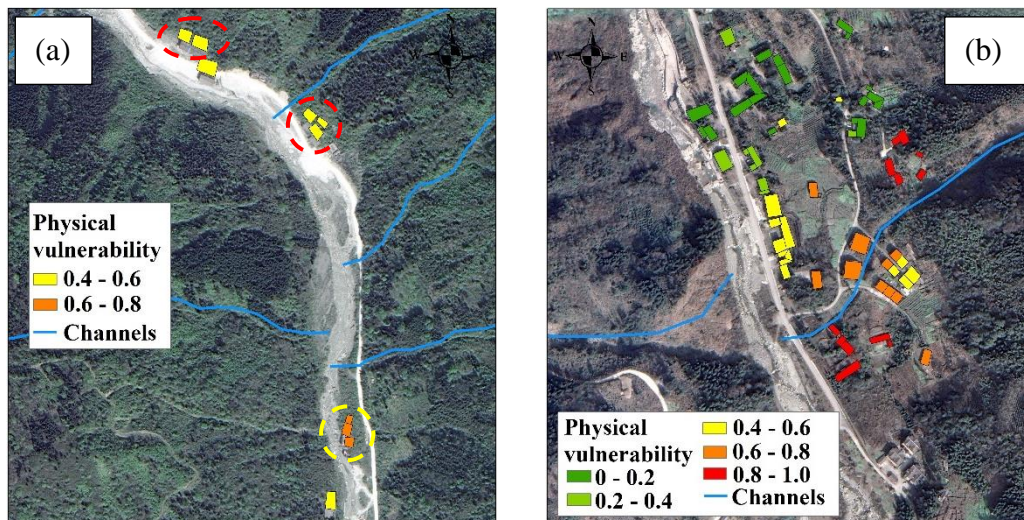
364 Figure 10. The residential areas (a), (b), (d), and (e) in the Longxihe Basin with highlighted buildings  
365 and (c) the debris-flow catchments that were prepared for the establishment of impact pressure

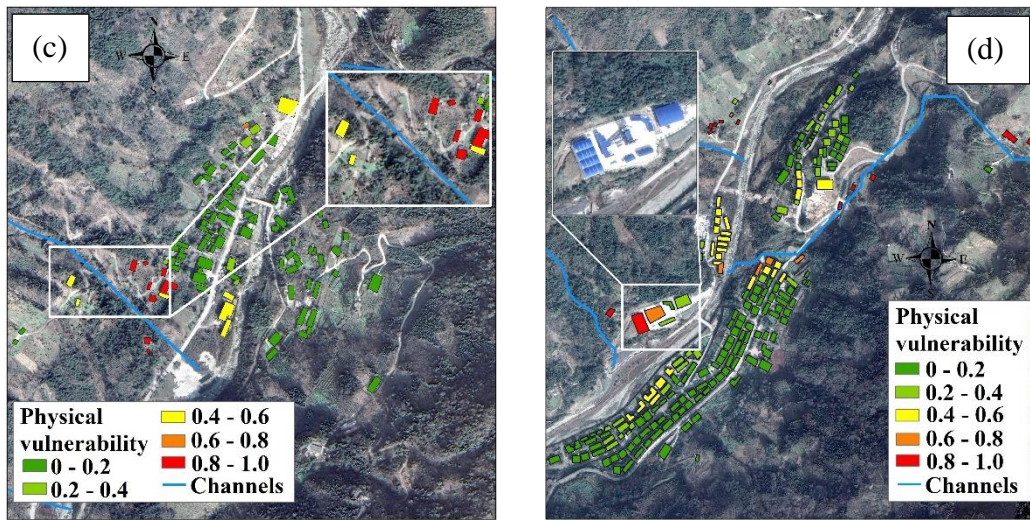


367 Table 3. Prediction results using developed prediction model

No.	$A / \text{km}^2$	$L / \text{km}$	$R / \text{m}$	$J$	Predicted $P_t$ (kPa)
1	0.4226	0.70	116	0.3024	22.0
2	0.8849	1.00	123	0.3503	26.7
3	0.1447	0.25	113	0.4055	18.0
4	2.9068	0.91	145	0.1668	22.1
5	0.3637	0.58	125	0.2998	19.2
6	0.9317	0.88	130	0.2551	20.9
7	4.1780	1.84	141	0.0751	16.0
8	0.1632	0.61	117	0.3419	19.3
9	0.0932	0.69	112	0.3622	17.3
10	0.1087	0.69	112	0.3542	17.5
11	0.2355	0.73	159	0.6828	16.5
12	1.3027	1.46	145	0.3944	25.2
13	2.8095	1.30	158	0.2466	26.5
14	0.3802	0.89	129	0.4299	19.2
15	0.2177	0.70	136	0.5690	15.8
16	0.1529	0.84	162	0.6821	14.4
17	3.5789	2.23	153	0.3047	33.6
18	0.3179	0.69	127	0.5400	17.4
19	0.1970	0.74	96	0.4056	15.0
20	0.2201	0.90	110	0.4599	13.0

368 In addition to the predicted impact pressures to the buildings by the potential debris flows, the  
 369 horizontal and vertical distances between each building and the nearest debris-flow channel were  
 370 measured using GIS. As a result, the physical vulnerabilities of the buildings in Longxihe Basin can be  
 371 decided based on the proposed physical vulnerability matrix, and the results are shown in Figs. 11(a)-(d).





373

374 Figure 11. (a)-(d) Physical vulnerabilities of the buildings for residential areas of the Longxihe Basin  
 375 corresponding to Figs. 10(a), 10(b), 10(d), and 10(e)

376

Table 4. Statistical results of the buildings with different physical vulnerabilities

	0 - 0.2	0.2 - 0.4	0.4 - 0.6	0.6 - 0.8	0.8 - 1.0
Number	237	52	45	18	34
Percentage	61.4%	13.5%	11.6%	4.7%	8.8%

377

378

379

380

381

382

383

384

385

386

387

388

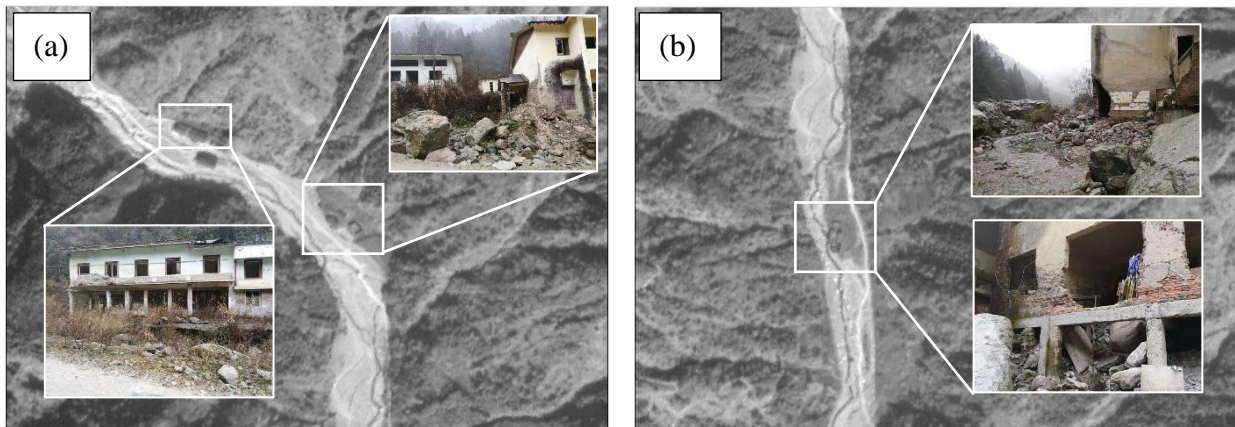
389

The statistical results in Table 4 illustrate that most buildings nearly suffer no damage when a debris-flow event occurs. This is because these buildings are RC-frame structures, which allow them to stay undamaged or only suffer slight damage even though they are close to the debris-flow channels. However, non-RC frame buildings may always suffer severe damage during a debris-flow event if their locations are near the channels. As indicated in Figs. 11(a)-(d), the buildings with high and very-high physical vulnerabilities are mainly brick and light steel structures. The difference in resistance ability allows a greater possibility for RC-frame buildings to keep structures undamaged during the same debris-flow event when compared to a non-RC building, which is consistent with the field investigation results in Fig. 4(b). Moreover, a non-RC frame building can also avoid damage even though it is close to the debris-flow channel. This is because a higher vertical distance to the debris-flow channel can allow this non-RC building to suffer no damage or light damage. Therefore, a comprehensive analysis by considering the structure type, spatial distances to debris-flow channel, and potential impact pressure is significant to establish a reliable physical vulnerability matrix to benefit the determination of the



390 potential damage degree of buildings.

391 In order to validate the efficiency and accuracy of our method in estimating the physical damages of  
392 buildings, the damaged buildings caused by debris flows on 13th August 2010 are employed here to  
393 assess the reliability of this method. As depicted in Fig. 12(a), the RC-frame buildings suffer a moderate  
394 damage (see red dashed circles in Fig. 11(a)) because there are no obvious damages of external or  
395 internal walls observed during the field investigations based on the HAZUS building classification  
396 scheme (Rojahn, 1988). However, the debris-flow event caused extensive damage (see yellow dashed  
397 circles in Fig. 11(a)) to the brick structures due to the partly destroyed external or internal walls (Fig.  
398 12(b)). As a result, evacuation of people is necessary and reconstruction is required. Overall, our  
399 proposed method can provide a reliable evaluation of physical vulnerability of buildings caused by a  
400 debris-flow event and therefore benefit their estimation of economic loss.



401

402 Figure 12. (a) The RC-frame buildings which suffered moderate damage with no obvious damage of  
403 external and internal walls found caused by a debris-flow event on 13 August 2010, and (b) extensive  
404 damage was observed on the brick buildings (non-RC frame structure) during the same debris-flow  
405 event.

#### 406 4.2.2 Economic loss

407 Based on the estimated physical damage, we can further provide a reliable estimation of the  
408 economic loss. Six categories of buildings were identified in this study area based on the field

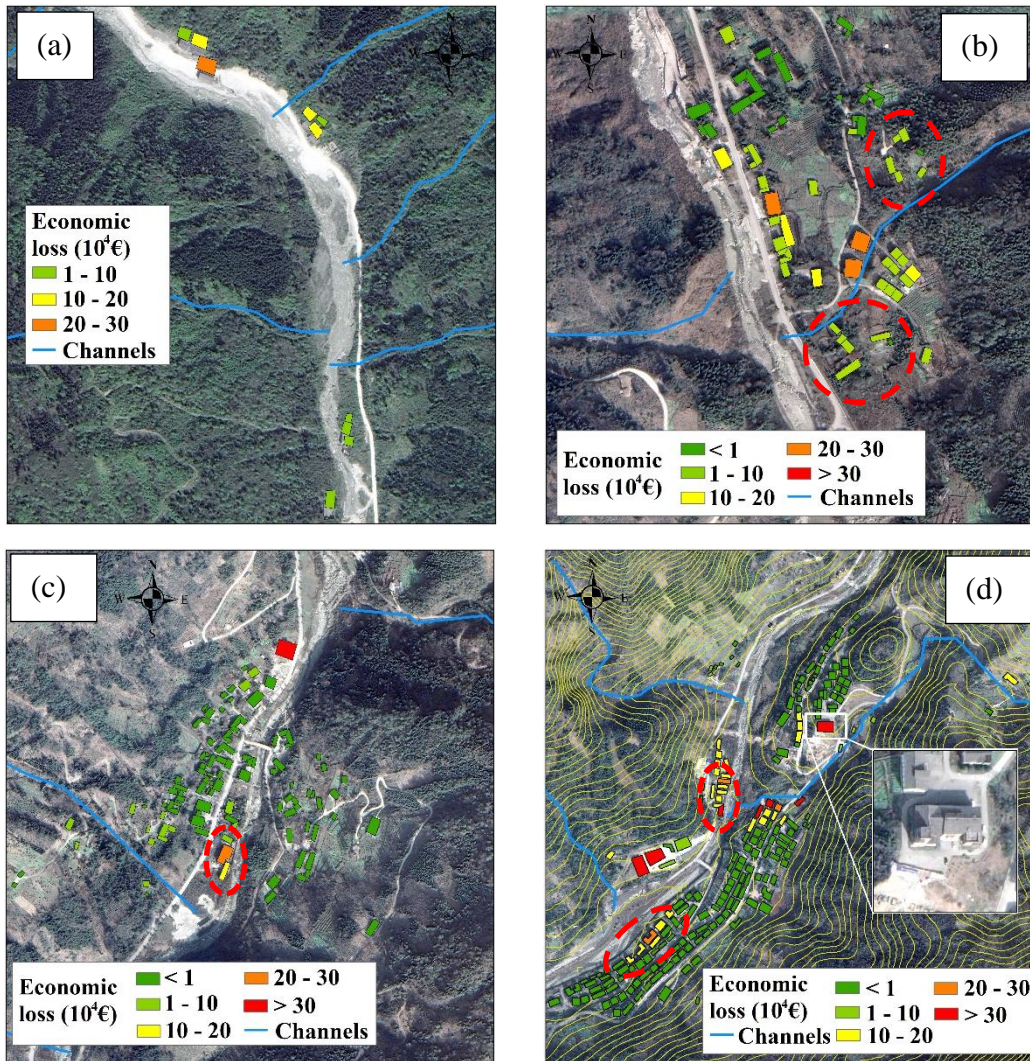
409 investigations. They are residential buildings, factory buildings, office buildings, and livestock houses.

410 Table 5. Unit price ( $P$ ) of a building in this area

Element	Categories	Unit price	Value based on
Buildings	Residential buildings (RC-frame)	1050.44 €/m <sup>2</sup>	Average market price
	Residential buildings (Brick structure)	158.38 €/m <sup>2</sup>	Construction cost
	Business buildings (RC-frame)	1371.47 €/m <sup>2</sup>	Average market price
	Office buildings (RC-frame)	1050.44 €/m <sup>2</sup>	\
	Factory buildings (Light steel structure)	237.57 €/m <sup>2</sup>	Construction cost
	Livestock houses (Brick structure)	7.92 €/m <sup>2</sup>	Restoration and reconstruction cost

411 The economic value of a residential building in this area is based on the market price, which is  
412 provided by the Housing and Urban-rural Construction Agency. As for the unit price of a business  
413 building, we refer to the price ratio of a residential building and a business building in the city center of  
414 Dujiangyan. The unit price of a business building is normally 30% higher than a residential building. An  
415 office building belongs to the national assets, which cannot be rented or sold. However, possible damage  
416 still cannot be avoided if a debris-flow event occurs, which therefore requires restoration or  
417 reconstruction. Therefore, we refer to the unit price of a residential building to estimate the economic  
418 loss of an office building. Unlike the high construction cost and business value of a residential building  
419 and a business building, the construction cost of a factory building is low because of its light steel  
420 structure. Meanwhile, this kind of building is normally situated at a distance from the city center and  
421 residential areas, primarily to mitigate effects of noise and environmental pollution. Most importantly, a  
422 factory building invariably occupies a large area, potentially raising the construction cost when situated  
423 in the city center due to the exorbitant land prices. Considering the average market price of a factory  
424 building, we decide the unit price as 237.57 €/m<sup>2</sup>. Finally, the livestock house is still considered here  
425 since two villages are included in the analysis, and the livestock house is built for sheep and cattle.  
426 Therefore, the unit price of a livestock building is low (see Table 5). The economic loss of the buildings

427 in the Longxihe Basin are presented in Fig. 13.



430 Figure 13. (a)-(d) Estimated economic loss of the buildings for residential areas of the Longxihe Basin  
431 corresponding to Figs. 10(a), 10(b), 10(d), and 10(e)

432 The distribution characteristics of economic loss are different from physical vulnerability. For  
433 example, Fig. 11(a) illustrates that the buildings are more likely to suffer severe damage if they are close  
434 to the debris-flow channel, especially the non-RC frame structures. However, these non-RC frame  
435 buildings require lower reconstruction or restoration costs when compared to the RC-frame buildings  
436 (see Fig. 13(a)). In this case, the economic loss is low since it relies on the multiplication of physical  
437 vulnerability and economic value of a building (see red dashes in Fig. 13(b)). As indicated in Fig. 13(d),  
438 the factory buildings (see Fig. 11(d) and Fig. 13(d)) may suffer an economic loss of  $3.2 \times 10^5 \text{ €}$ . As for

439 the reason why a low unit price of a factory building (see Table 5) results in a high economic loss may  
440 be due to the large area of this factory building. Therefore, the site selection of a factory building is  
441 significant. Although the location of the factory buildings in mountainous areas can avoid noise  
442 pollution in urban development and decrease construction costs, the possible economic loss caused by  
443 natural hazards cannot be neglected. Additionally, the residential building should not be built on the  
444 outlet of the debris-flow catchment directly opposite (see red dash circles in Fig. 13(d)), especially when  
445 the foundation of the residential buildings is only slightly higher than the riverway (see yellow contours  
446 in Fig. 13(d)). For example, the highest economic loss is found in a residential building (see the image in  
447 Fig. 13(d)), reaching  $5.1 \times 10^5$  €. Therefore, at least a 4 m of residential building (RC frame) foundation  
448 is essential if the buildings are close to the debris-flow channel based on Table 2. Overall, the analysis of  
449 economic loss for buildings in mountainous areas can provide decision-makers with guidance about  
450 urban planning.

## 451 **5. Discussion**

452 The proposed integrated method has been applied for the determination of the damage degree for  
453 buildings in the Longxihe Basin, Sichuan, China. The involvement of debris-flow intensities, building  
454 attributes, and spatial position between the buildings and debris-flow channel can help to suggest a more  
455 reasonable damage degree value caused by debris flows. Specifically, the debris-flow intensity is  
456 expressed in impact pressure here, which can indicate the possible consequence of a building if the  
457 flowing materials strike the building directly. However, an overestimation of the damage degree may be  
458 caused since the spatial positions between the building and debris-flow channel is not a one-dimensional  
459 problem. In general, the elevation of a building is greater than that of the debris-flow channel in the  
460 horizontal direction. This is because the long-term water flow and historical debris flows move the soils  
461 and rocks, causing erosion of the channel bottom and therefore decreasing its elevation. As a result, the

462 elevation difference between the buildings and the debris-flow channel could cause a loss of impact  
463 pressure. Therefore, simply utilizing impact pressure is not enough to reflect the actual damage to a  
464 building. In contrast, the introduction of *HD* and *VD* is an effective supplement to improve the  
465 estimation of physical damage that the buildings may suffer. Furthermore, the damage degree may vary  
466 when subjected to different building structures. In this case, two major types of buildings are considered  
467 in this study to distinguish the impact resistance capacities of different building types. Overall, this  
468 developed matrix comprehensively describes the factors impacting the damage degree of buildings  
469 caused by debris flows.

470 By utilizing the proposed matrix, we can estimate the damage degree of a building. However, the  
471 possible damage in future scenarios is still unclear due to the change in debris-flow magnitude.  
472 Therefore, an ensemble machine learning (ML) model is used to predict the volume of a future debris-  
473 flow event so that the debris-flow intensities can be calculated based on the empirical relationships. This  
474 ML method can effectively avoid over-fitting when training prediction models due to the existence of a  
475 regular term. Most importantly, the strong ability in establishing a reliable relationship between a group  
476 of independent variables and a dependent variable enables a wider application of ML methods when  
477 compared to empirical and regression methods. Therefore, a precise prediction can be expected based on  
478 the established relationship using the ML method to indicate the potential damage to buildings caused by  
479 a future debris-flow event. However, we are also aware that the current sample size may not support a  
480 robustness performance in estimating impact pressure to buildings. For broader applications, continuous  
481 input of debris-flow data globally is essential, which may be beyond the scope of this study. However,  
482 further improvement can also be achieved if the floors of buildings are considered when developing the  
483 physical vulnerability matrix. This is because the degree of loss presents a negative correlation with the  
484 number of floors (Fuchs et al., 2019). Nevertheless, the limitation cannot alter the fact that our work can



485 benefit the subdivision of buildings in different vulnerability levels and provide suggestions about the  
486 site selection of future residential areas.

## 487 **6. Conclusion**

488 In this paper, an integrated method for vulnerability assessment of buildings caused by future debris  
489 flows was proposed. This method includes a physical matrix and a machine learning model, in which  
490 this matrix was developed by considering the debris-flow process, building structure, and spatial  
491 positions between the buildings and debris-flow channels. To be more specific, the debris-flow process  
492 is represented by impact pressure ( $P_t$ ), which can be estimated based on the debris-flow volume through  
493 field investigations. As for the definition of spatial positions,  $HD$  and  $VD$  are used to describe the  
494 position relation between the buildings and the debris-flow channel. By combining the three parameters,  
495 the actual impact pressure on the buildings can be decided. However, the damage degree may vary for  
496 different building structures. Therefore, the building structure is further considered to provide a precise  
497 estimation of the buildings, including the RC frame and non-RC frame (brick structure, light steel  
498 structure, and masonry structure). Therefore, a total of six types of buildings are included in this study.  
499 They are residential buildings (RC frame and brick structure), business buildings (RC frame), office  
500 buildings (RC frame), factory buildings (light steel structure), and livestock houses (brick structure). At  
501 the same time, an ML model (XGBoost) was developed to predict the impact pressure to buildings  
502 caused by future debris flows. On the basis of the proposed physical vulnerability matrix and machine  
503 learning model, we selected the Longxihe Basin, Sichuan, China, to conduct a case study. The results  
504 show that the non-RC buildings may be more likely to suffer severe damage if they are close to the  
505 debris-flow channels. The buildings with high and very-high physical vulnerabilities are mainly brick  
506 and light steel structures. Consequently, the factory buildings occupy the highest economic loss,  
507 reaching  $2.41 \times 10^5$  € due to their large area. In addition, the buildings may suffer severe economic loss if

508 they are located the directly opposite of the outlet of the debris-flow catchment. Overall, our studies can  
509 achieve a reliable assessment of the physical damage and corresponding economic loss of buildings and  
510 therefore provide suggestions and scientific support for the future construction planning of buildings.

#### 511 **Code/Data availability**

512 All raw data will be provided on request.

#### 513 **CRedit authorship contribution statement**

514 **Chenchen Qiu:** Methodology, Software, Data curation, Writing - Original draft preparation. **Xueyu**  
515 **Geng:** Conceptualization, Visualization, Validation, Supervision, Writing – Review & Editing.

#### 516 **Declaration of competing interest**

517 The authors declare that they have no known competing financial interests or personal relationships  
518 that could have appeared to influence the work reported in this paper.

#### 519 **Acknowledgement**

520 This work is financially supported by the European Union's Horizon 2020 research and innovation  
521 program Marie Skłodowska–Curie Actions Research and Innovation Staff Exchange (RISE) under grant  
522 agreement [grant number 778360].

523 For the purpose of open access, the author has applied a Creative Commons Attribution (CC-BY)  
524 licence to any Author Accepted Manuscript version arising from the submission.

#### 525 **References**

- 526 Alene, G.H., Irshad, S., Moraru, A., Depina, I., Bruland, O., Perkis, A. and Thakur, V., 2024. Virtual  
527 reality visualization of geophysical flows: A framework. *Environmental Modelling & Software*, 177,  
528 p.106063.
- 529 Bründl, M., Romang, H.E., Bischof, N., Rheinberger, C.M., 2009. The risk concept and its application in  
530 natural hazard risk management in Switzerland. *Nat. Hazards Earth Syst. Sci.* 9, 801–813.
- 531 Chang, M., Tang, C., Zhang, D.D. and Ma, G.C., 2014. Debris flow susceptibility assessment using a  
532 probabilistic approach: A case study in the Longchi area, Sichuan province, China. *Journal of*  
533 *Mountain Science*, 11, pp.1001-1014.
- 534 Chang, M., Tang, C., Ni, H. and Qu, Y., 2015. Evolution process of sediment supply for debris flow

- 535 occurrence in the Longchi area of Dujiangyan City after the Wenchuan earthquake. *Landslides*, 12,  
536 pp.611-623.
- 537 Chen, T., Guestrin, C., 2016. XGBoost: A scalable tree boosting system. *Proc. ACM SIGKDD Int. Conf.*  
538 *Knowl. Discov. Data Min.* 13-17-Aug, 785–794. <https://doi.org/10.1145/2939672.2939785>
- 539 Creutin, J.D., Muste, M., Bradley, A.A., Kim, S.C., Kruger, A., 2003. River gauging using PIV  
540 techniques: A proof of concept experiment on the Iowa River. *J. Hydrol.* 277, 182–194.  
541 [https://doi.org/10.1016/S0022-1694\(03\)00081-7](https://doi.org/10.1016/S0022-1694(03)00081-7)
- 542 Cui, P., Xiang, L.Z., Zou, Q., 2013. Risk assessment of highways affected by debris flows in Wenchuan  
543 earthquake area. *J. Mt. Sci.* 10, 173–189. <https://doi.org/10.1007/s11629-013-2575-y>
- 544 Dai, F.C., Lee, C.F., Ngai, Y.Y., 2002. Landslide risk assessment and management: An overview. *Eng.*  
545 *Geol.* 64, 65–87. [https://doi.org/10.1016/S0013-7952\(01\)00093-X](https://doi.org/10.1016/S0013-7952(01)00093-X)
- 546 Fell, R., 1994. Landslide risk assessment and acceptable risk. *Can. Geotech. J.* 31, 261–272.
- 547 Fuchs, S., 2009. Susceptibility versus resilience to mountain hazards in Austria-paradigms of  
548 vulnerability revisited. *Nat. Hazards Earth Syst. Sci.* 9, 337–352.
- 549 Fuchs, S., Keiler, M., Ortlepp, R., Schinke, R., Papathoma-Köhle, M., 2019. Recent advances in  
550 vulnerability assessment for the built environment exposed to torrential hazards: Challenges and the  
551 way forward. *J. Hydrol.* 575, 587–595.
- 552 Guzzetti, F., Stark, C.P., Salvati, P., 2005. Evaluation of flood and landslide risk to the population of  
553 Italy. *Environ. Manage.* 36, 15–36.
- 554 Huang, J., Hales, T.C., Huang, R., Ju, N., Li, Q., Huang, Y., 2020. A hybrid machine-learning model to  
555 estimate potential debris-flow volumes. *Geomorphology* 367, 107333.  
556 <https://doi.org/10.1016/j.geomorph.2020.107333>
- 557 Immerzeel, W.W., Lutz, A.F., Andrade, M., Bahl, A., Biemans, H., Bolch, T., Hyde, S., Brumby, S.,



558 Davies, B.J., Elmore, A.C. and Emmer, A., 2020. Importance and vulnerability of the world's water  
559 towers. *Nature*, 577(7790), pp.364-369.

560 Institute of Mountain Hazards and Environment (IMHE) (1994) Flood, Debris flow, landslide hazard  
561 and control. Science Publications. ((in Chinese))

562 Jakob, M., Stein, D., Ulmi, M., 2012. Vulnerability of buildings to debris flow impact. *Nat. Hazards* 60,  
563 241–261. <https://doi.org/10.1007/s11069-011-0007-2>

564 Jiang, H., Zou, Q., Zhu, Y., Li, Y., Zhou, B., Zhou, W., Yao, S., Dai, X., Yao, H. and Chen, S., 2024.  
565 Deep Learning Prediction of Rainfall-driven Debris Flows Considering the Similar Critical  
566 Thresholds within Comparable Background Conditions. *Environmental Modelling & Software*,  
567 p.106130.

568 Kang, H. sub, Kim, Y. tae, 2016. The physical vulnerability of different types of building structure to  
569 debris flow events. *Nat. Hazards* 80, 1475–1493. <https://doi.org/10.1007/s11069-015-2032-z>

570 Khosravi, K., Khozani, Z.S., Mao, L., 2021. A comparison between advanced hybrid machine learning  
571 algorithms and empirical equations applied to abutment scour depth prediction. *J. Hydrol.* 596,  
572 126100. <https://doi.org/10.1016/j.jhydrol.2021.126100>

573 Koch, T., 1998. Testing various constitutive equations for debris flow modelling. *IAHS-AISH Publ.*  
574 249–257.

575 Liu, S., Wei, L., Hu, K., 2020. Topographical and geological variation of effective rainfall for debris-  
576 flow occurrence from a large-scale perspective. *Geomorphology* 358, 107134.

577 Marcato, G., Bossi, G., Rivelli, F., Borgatti, L., 2012. Debris flood hazard documentation and mitigation  
578 on the Tilcara alluvial fan (Quebrada de Humahuaca, Jujuy province, North-West Argentina). *Nat.*  
579 *Hazards Earth Syst. Sci.* 12, 1873–1882. <https://doi.org/10.5194/nhess-12-1873-2012>

580 Miao, C., Liu, X., 2020. Characterization of acceptable risk for debris flows in China: Comparison in

581 debris-flow prone areas and nonprone areas. *Int. J. disaster risk Reduct.* 42, 101405.

582 Papathoma-Köhle, M., Gems, B., Sturm, M., Fuchs, S., 2017. Matrices, curves and indicators: A review  
583 of approaches to assess physical vulnerability to debris flows. *Earth-Science Rev.* 171, 272–288.

584 Paudel, B., Fall, M., Daneshfar, B., 2021. Gis-Based Assessment of Debris Flow Runout in Kulekhani  
585 Watershed, Nepal. *Geotech. Geol. Eng.* 39, 2755–2775. [https://doi.org/10.1007/s10706-020-01655-](https://doi.org/10.1007/s10706-020-01655-1)  
586 1

587 Qiu, C., Su, L., Zou, Q., Geng, X., 2022. A hybrid machine-learning model to map glacier-related debris  
588 flow susceptibility along Gyirong Zangbo watershed under the changing climate. *Sci. Total Environ.*  
589 818, 151752. <https://doi.org/10.1016/j.scitotenv.2021.151752>

590 Qiu, C., Su, L., Zou, Q., Geng, X., 2022. An AI-based method for estimating the potential runout  
591 distance of post-seismic debris flows. *International Journal of Disaster Risk Science*, pp, 1-14.

592 Quan Luna, B., Blahut, J., Van Westen, C.J., Sterlacchini, S., Van Asch, T.W.J., Akbas, S.O., 2011. The  
593 application of numerical debris flow modelling for the generation of physical vulnerability curves.  
594 *Nat. Hazards Earth Syst. Sci.* 11, 2047–2060. <https://doi.org/10.5194/nhess-11-2047-2011>

595 Rickenmann, D., 1999. Empirical relationships for debris flows. *Nat. Hazards* 19, 47–77.  
596 <https://doi.org/10.1023/A:1008064220727>

597 Rojahn, C., 1988. Rapid visual screening of buildings for potential seismic hazards: A handbook.  
598 Federal Emergency Management Agency.

599 Ruggieri, S., Calò, M., Cardellicchio, A., Uva, G., 2022. Analytical-mechanical based framework for  
600 seismic overall fragility analysis of existing RC buildings in town compartments. *Bull. Earthq. Eng.*  
601 20, 8179–8216.

602 Ruggieri, S., Liguori, F.S., Leggieri, V., Bilotta, A., Madeo, A., Casolo, S., Uva, G., 2023. An  
603 archetype-based automated procedure to derive global-local seismic fragility of masonry building

604 aggregates: META-FORMA-XL. *Int. J. disaster risk Reduct.* 95, 103903.

605 Santi, P.M., Hewitt, K., VanDine, D.F., Barillas Cruz, E., 2011. Debris-flow impact, vulnerability, and  
606 response. *Nat. hazards* 56, 371–402.

607 Sridharan, A., Gutjahr, G. and Gopalan, S., 2024. Markov–Switching Spatio–Temporal Generalized  
608 Additive Model for Landslide Susceptibility. *Environmental Modelling & Software*, 173, p.105892.

609 Sturm, M., Gems, B., Keller, F., Mazzorana, B., Fuchs, S., Papathoma-Köhle, M., Aufleger, M., 2018.  
610 Understanding impact dynamics on buildings caused by fluvial sediment transport.  
611 *Geomorphology* 321, 45–59. <https://doi.org/10.1016/j.geomorph.2018.08.016>

612 Wei, L., Hu, K., Hu, X., 2018. Rainfall occurrence and its relation to flood damage in China from 2000  
613 to 2015. *J. Mt. Sci.* 15, 2492–2504.

614 Wei, L., Hu, K., Liu, J., 2022. Automatic identification of buildings vulnerable to debris flows in  
615 Sichuan Province, China, by GIS analysis and Deep Encoding Network methods. *J. Flood Risk*  
616 *Manag.* 15, 1–18. <https://doi.org/10.1111/jfr3.12830>

617 Xie, H., Liu, W., Zhao, J., Hu, K., 2013. Characteristics of Tangjiagou debris flow in Shimian of  
618 Sichuan in July 14, 2012. *J. Earth Sci. Environ.* 35, 90–97.

619 Yu, B., Ma, Y., Zhang, J.N., Wu, Y.F., Zhang, H.H., Li, L., Chu, S.M. and Qi, X., 2011. The group  
620 debris flow hazards after the Wenchuan earthquake in Longchi, Dujiangyan, Sichuan Province.  
621 *Journal of Mountain Science*, 29(6), pp.738-746.

622 Yu, B., Wu, Y., Chu, S., 2014. Preliminary study of the effect of earthquakes on the rainfall threshold of  
623 debris flows. *Eng. Geol.* 182, 130–135. <https://doi.org/10.1016/j.enggeo.2014.04.007>

624 Zanchetta, G., Sulpizio, R., Pareschi, M.T., Leoni, F.M., Santacroce, R., 2004. Characteristics of May 5–  
625 6, 1998 volcaniclastic debris flows in the Sarno area (Campania, southern Italy): relationships to  
626 structural damage and hazard zonation. *J. Volcanol. Geotherm. Res.* 133, 377–393.

627 Zhang, S., Zhang, L., Li, X., Xu, Q., 2018. Physical vulnerability models for assessing building damage  
628 by debris flows. *Eng. Geol.* 247, 145–158.

629

630 **Appendix. A**

631 1. Mechanism of XGBoost

632 The mechanism of XGBoost is to constantly develop a new decision tree which acts as a weak  
 633 learner and fits the residual error of the last prediction. After the training of a total of  $k$  trees, the final  
 634 prediction result is the sum of the score of each leaf node in each developed tree. The target function of  
 635 regression in XGBoost is:

$$636 \quad L(\phi) = \sum_{i=1}^m l(y_i, y_i) + \sum_{k=1}^t \Omega(f_k) \quad (10)$$

637 where  $\sum_{i=1}^m l(y_i, y_i)$  represents the loss function, and  $\sum_{k=1}^t \Omega(f_k)$  is the regularisation term.  $y_i$  and  $y_i$   
 638 are prediction value and true value, respectively.  $m$  is the number of samples.  $f_k$  is the  $k$ th tree model. As  
 639 mentioned above, the newly generated tree needs to fit the residual error of the last prediction, and  
 640 therefore the prediction result can be presented as:

$$641 \quad y_i^t = y_i^{(t-1)} + f_t(x_i) \quad (11)$$

642 Substitute the Eq. (12) into Eq. (11) to rewrite the objective function as:

$$643 \quad L(\phi) = \sum_{i=1}^m l\left(y_i, y_i^{(t-1)} + f_t(x_i)\right) + \sum_{k=1}^t \Omega(f_k) \quad (12)$$

644 Furthermore, Taylor's second order expansion is introduced to find  $f_k$  to minimize the objective  
 645 function:

$$646 \quad L(\phi) = \sum_{i=1}^m \left[ l\left(y_i, y_i^{(t-1)}\right) + g_i f_t(x_i) + \frac{1}{2} h_i f_t^2(x_i) \right] + \sum_{k=1}^t \Omega(f_k) + constant \quad (13)$$

647 where  $g_i$  is the first derivation, and the  $h_i$  represents the second derivation

648 2. Calculation results of impact pressure  $P_t$

649 Table A1. Dataset II for developing the impact pressure prediction model

No.	A	L	R	J	$P_t$	No.	A	L	R	J	$P_t$
	(km <sup>2</sup> )	(km)	(m)		(kPa)		(km <sup>2</sup> )	(km)	(m)		(kPa)
1	8.55	3.13	269	0.1051	40.9	42	0.05	0.18	85	0.1908	10.3
2	4.68	1.41	126	0.2162	47.4	43	0.06	0.23	81	0.3038	14.2

3	12.88	4.16	269	0.1246	56.0	44	0.33	0.50	162	0.2792	18.4
4	0.29	0.50	95	0.1638	13.2	45	0.05	0.20	107	0.2661	12.2
5	0.29	0.29	200	0.4122	23.0	46	1.37	1.11	160	0.1763	34.1
6	5.73	0.71	260	0.1175	49.4	47	4.83	1.96	277	0.2071	35.5
7	0.56	0.62	195	0.2475	29.3	48	1.33	0.50	258	0.5117	35.7
8	2.15	0.73	250	0.2736	24.2	49	0.17	0.62	231	0.4727	21.0
9	0.32	0.46	276	0.5452	23.0	50	12.47	3.61	366	0.1853	67.9
10	1.67	0.95	161	0.3699	32.3	51	0.46	0.88	189	0.3819	26.4
11	11.21	1.93	360	0.1512	34.1	52	1.63	1.98	148	0.3115	28.9
12	2.85	1.57	232	0.2568	28.3	53	1.34	1.00	158	0.1727	18.7
13	2.29	1.84	189	0.3581	46.6	54	0.24	0.43	151	0.2867	16.6
14	0.08	0.42	240	0.3561	16.6	55	0.39	0.75	120	0.1745	15.6
15	0.18	0.48	366	0.6976	13.0	56	0.02	0.1	132	0.5295	18.0
16	0.53	0.81	170	0.2943	22.5	57	2.56	1.23	127	0.0998	16.7
17	0.71	1.74	151	0.6494	166.9	58	1.62	0.71	229	0.1673	19.7
18	0.49	1.64	162	0.6494	181.2	59	0.49	1.41	182	0.3000	24.0
19	0.60	1.52	155	0.6469	155.1	60	0.21	0.66	215	0.5384	40.6
20	0.36	1.15	261	0.8214	127.6	61	0.29	1.31	133	0.5184	64.1
21	2.73	2.57	190	0.6771	88.2	62	0.85	1.75	163	0.4578	36.0
22	2.02	2.59	198	0.7028	94.9	63	1.71	2.06	145	0.3879	68.5
23	0.43	1.30	198	0.7729	94.7	64	1.27	2.16	183	0.3522	84.1
24	0.19	1.09	181	0.6873	79.2	65	0.89	2.07	127	0.3385	68.1
25	1.03	2.02	232	0.4369	51.2	66	0.49	1.20	168	0.5681	141.0
26	3.99	3.78	134	0.4061	36.8	67	0.75	1.58	327	0.5566	165.7
27	2.88	2.40	313	0.7107	66.5	68	0.37	0.52	199	0.3404	23.6
28	0.34	1.14	163	0.8571	102.6	69	0.77	0.76	115	0.1566	17.0
29	2.81	2.84	253	0.5250	80.8	70	0.31	0.87	178	0.1317	25.9
30	7.18	4.82	400	0.5139	102.4	71	0.36	0.35	261	0.4578	20.6
31	24.42	9.47	337	0.3153	20.2	72	2.62	1.39	321	0.3482	33.8
32	2.81	1.74	205	0.3191	31.8	73	0.84	1.39	199	0.4899	14.9
33	0.43	1.30	200	0.8012	47.5	74	2.72	2.56	528	0.1069	31.2
34	7.06	4.41	275	0.4473	84.1	75	5.85	0.86	365	0.2962	31.5
35	1.07	2.05	225	0.4431	71.0	76	2.61	1.28	388	0.5317	44.0
36	0.86	2.17	149	0.3979	70.6	77	5.45	2.82	261	0.5228	112.0
37	6.51	2.92	252	0.5029	110.7	78	3.51	0.99	227	0.3839	38.2
38	0.42	1.64	151	0.4813	149.0	79	7.09	2.29	293	0.1962	52.6
39	0.51	1.43	153	0.4899	153.1	80	0.02	0.21	110	0.4390	17.8
40	0.20	0.76	130	0.5520	51.6	81	2.06	1.92	160	0.3211	29.7
41	0.34	1.25	130	0.4942	56.5						

650

651